Culha, C., Schroeder, D. M., Jordan, T. M., & Haynes, M. S. (2020). Assessing the detectability of Europa's eutectic zone using radar sounding. *Icarus*, *339*, [113578]. https://doi.org/10.1016/j.icarus.2019.113578

Assessing the Detectability of Europa's Eutectic Zone Using Radar Sounding

Cansu Culha [a], Dustin M Schroeder[a,b], Thomas M Jordan[a,c], Mark S Haynes[d]

[a]*Stanford University Department of Geophysics, 397 Panama Mall, Stanford, CA 94305-2115, USA. Email: cculha@stanford.edu*
[b]*Department of Electrical Engineering, Stanford University, Stanford, CA*
[c]*School of Geographical Sciences, University of Bristol, Bristol, UK.*
[d]*Jet Propulsion Laboratory (JPL), California Institute of Technology, Pasadena, CA*

Abstract

Radar sounding is a geophysical method capable of directly imaging subsurface interfaces within the ice shell of the icy moons, including Jupiter's moon, Europa. For this reason, both the European Space Agency's JUpiter ICy moons Explorer and the National Aeronautics and Space Administration's Europa Clipper missions have ice penetrating radar sounders in their payloads. In addition to the ice-ocean interface and shallow water lenses, liquid water in the eutectic zone of Europa's ice shell could also be a target for radar sounding investigations. However, the wide range of possible configurations for eutectic-zone water bodies and the overlying ice make their absolute echo strength difficult to predict. To address this challenge, we employ a suite of simple water configurations and scattering models to bound the eutectic detectability in terms of its effective reflectivity. We find that, for each configuration, a range of physically plausible eutectic parameters exist that could produce detectable echoes, with effective reflectivity values greater than -50 dB at HF or VHF frequencies.

Keywords: EUROPA, EUTECTIC, RADAR, WATER

1. Introduction

The surface of Jupiter's moon Europa has a myriad of features suggesting a dynamic and complex ice shell (e.g., Pappalardo and Sullivan, 1996; McEwen and Bierhaus, 2006;

Singer et al., 2010; Culha and Manga, 2016). To investigate the physical properties of this ice shell, two upcoming missions are planned to carry ice penetrating radar sounders: the European Space Agency's (ESA's) JUpiter ICy moons Explorer (JUICE) (Grasset et al., 2013) and the National Aeronautics and Space Administration's (NASA's) Europa Clipper Mission (Phillips and Pappalardo, 2014). The JUICE mission payload includes the Radar for Icy Moon Exploration (RIME) (Bruzzone et al., 2013) and the Europa Clipper mission includes the Radar for Europa Assessment and Sounding: Ocean to Near-surface (REASON) (Blankenship et al., 2009). RIME is planned to operate in a single frequency band centered at 9 MHz with a bandwidth of 3 MHz (Bruzzone et al., 2015) and REASON is planned to operate a dual frequency system with a High Frequency (HF) band centered at 9 MHz with a bandwidth of 1 MHz and a Very High Frequency (VHF) band centered at 60 MHz with a bandwidth of 10 MHz (Blankenship et al., 2009; Grima et al., 2015).

These radar sounders have the potential to image subsurface features within the ice shell including the ice/ocean interface (Moore, 2000) and shallow water bodies (e.g., Schmidt et al., 2011). Additionally, water bodies in the eutectic zone of Europa's ice shell (Kalousová et al., 2017; Heggy et al., 2017) could serve as radar sounding targets. The eutectic zone is the portion of the ice shell with pressures and temperatures that allow both the liquid and solid phases of water to exist. For Europan ice shell thicknesses less than 30 km, this zone is expected to exist between 4 and 20 km below the surface depending on the chemical, thermal, and physical properties of the ice shell (Kalousová et al., 2017; McCarthy et al., 2007). Because they originate midway through the ice shell, radar echoes from the eutectic zone experience less attenuation than echoes from the ice/ocean interface (Kalousová et al., 2017). However, even with this reduced attenuation, water bodies in the eutectic zone can serve as radar sounding targets only if they also produce reflections with sufficient strength. In this paper, we use a suite of three simple models for the configuration of water in the eutectic zone to explore the range of parameters for which detectable echoes could be produced.

Radar sounding link budgets (e.g., Di Paolo et al., 2014; Blankenship et al., 2009; Bruzzone et al., 2015) are often based on specular ice-water reflectors (Schroeder et al., 2015) such as the ice-ocean interface or shallow water lenses (e.g. Schmidt et al., 2011) or specular internal density/conductivity layers (Cavitte et al., 2016; Smith et al., 2016). However, liquid water at the eutectic may not occur as a sharp transition from ice to a reflecting liquid water layer. It may, for example, include a homogeneous mixture of ice and water (Case 1), a gradual gradient in water content (Case 2), or a collection of small scattering liquid water pores (Case 3). Each of these departures from specular reflection would result in weaker radar echos. Therefore, to assess the impact such configurations have on eutectic detectability, we investigate three simple end-member configurations and their effect on radar scattering. We compare these to the baseline case of the specular reflections to provide an "effective reflectivity" value for each configuration that can be subtracted from any given link budget (e.g. Di Paolo et al., 2017; Blankenship et al., 2009; Haynes et al., 2018) or ice shell propagation/attenuation model (e.g. Kalousová et al., 2017; Heggy et al., 2017). This allows us to focus our analysis on the specific dependence of reflection strength on the eutectic geometry. We identify that the parameters that would alter our ability to detect the eutectic zone in the 3 cases are liquid volume fraction, or porosity, the gradient of porosity, and the liquid pore sizes, or pore size. Along with assessing our ability to detect the eutectic zone, we also explore what information can be teased out of the radar sounders.

2. Methods

Radar sounding is a powerful geophysical tool to detect and characterize features within an ice shell (McKinnon, 2005; Blankenship et al., 2009; Heggy et al., 2012; Bruzzone et al., 2015; Di Paolo et al., 2017; Kalousová et al., 2017). As electromagnetic pulses from a radar sounder travel through an ice shell, they reflect, scatter, and attenuate during propagation (Gudmandsen, 1971). The returned echoes provide an image of dielectric horizons within the ice shell. The received power due to reflection from a sharp interface between ice and liquid water can be modeled as a specular Fresnel reflection so that

$$P_r \propto \frac{\Gamma_o}{R^2} \tag{1}$$

where

$$\Gamma_o = \left| \frac{\sqrt{\varepsilon_l} - \sqrt{\varepsilon_i}}{\sqrt{\varepsilon_l} + \sqrt{\varepsilon_i}} \right|^2 \tag{2}$$

P_r is the received power, Γ_o is the power reflectivity, R is the range from the radar to the target, and ε_l and ε_i are the complex permittivities of liquid water and ice, respectively (Peters et al., 2005). We compare the three eutectic geometry cases described below to this specular reflection in order to determine the effective reduction of Γ from the baseline scenario. This "effective reflectivity" can be combined with link budget (e.g., Bruzzone et al., 2015) and attenuation (e.g., Kalousová et al., 2017; Di Paolo et al., 2014) calculations to evaluate the detectability of each eutectic configuration. We do not model the attenuation in the ice shell above the eutectic zone. Instead, we calculate the power return relative to a sharp reflection; therefore any variation above the eutectic zone that would lead to attenuation (such as temperature and chemical composition) would be equivalent in both the baseline scenario and our 3 cases.

2.1. Case 1: Sharp Interface:

The first configuration we consider is a 'mushy water layer'; a two-phase mixture of ice and liquid water that behaves as an effective medium. In this case, the permittivity of the layer is described by an effective permittivity, ε_{eff}, which replaces ε_l in eq. (2). The effective permittivity varies as a function of liquid water porosity, ϕ. When the size of the liquid water inclusions is negligible compared with the radar wavelength, a power-law mixing model of the form

$$\varepsilon_{eff}^{\alpha} = \phi\varepsilon_l^{\alpha} + (1-\phi)\varepsilon_i^{\alpha} \tag{3}$$

can be used to approximate the complex permittivity where α is a dimensionless parameter (Kärkkäinen et al., 2000; Wilhelms, 2005). Many applications of eq. (3) assume $\alpha = 3$

(the commonly used Looyenga mixing model) (e.g., Wilhelms, 2005). Here, following Di Paolo et al. (2014) and Kendrick et al. (2018) we assume $\alpha = 1$ (a linear mixing model). A discussion of this as a bound upon ε_{eff} is provided by Kärkkäinen et al. (2000).

We consider modelling reflections from two-phase mixtures of fresh, saline, or brine liquid water with ice. The complex permittivities are:

$$\begin{aligned} \varepsilon_i &= 3.17\ (1 - i0.0062) \\ \varepsilon_{l,f} &= 80\ (1 - i0.002) \\ \varepsilon_{l,s} &= 77\ (1 - i11.3) \\ \varepsilon_{l,b} &= 30\ (1 - i0.1), \end{aligned} \tag{4}$$

where $\varepsilon_{l,f}$, $\varepsilon_{l,s}$, and $\varepsilon_{l,b}$ are the permittivities of pure, saline and brine water, respectively (Neal, 1979; Peters et al., 2005; Pettinelli et al., 2016; Heggy et al., 2017) and $i = \sqrt{-1}$. Although complex permittivities are temperature dependent, the permittivity of ice, whether it is salty or pure, falls in the range of 3 – 3.8 between 100 – 250K (Pettinelli et al., 2016). In our analysis we use pure and salty liquid water as measured on Earth at 273K; however, semi-liquid water containing dense and contaminant-rich ice brines could potentially reduce the real part of the permittivity to values as low as $\varepsilon_{l,b}$ (Heggy et al., 2017). Following Gudmandsen (1971) and Schroeder et al. (2016), we assume ε_i, $\varepsilon_{l,f}$, $\varepsilon_{l,s}$, and $\varepsilon_{l,b}$ are the same for both the HF and VHF bands.

For a liquid porosity of unity, $\phi = 1$, this case becomes the baseline specular reflecting case against which we compare the effective reflectivity of other eutectic configurations. In Section 4.1, for $\phi = 1$, we demonstrate a small ($\sim$ 2.5 dB and 2 dB) reduction in baseline reflectivity between fresh and saline water and fresh and brine water, respectively. However, in the rest of the study we assume fresh water, and quantify the reduction in reflectivity relative to this baseline scenario.

2.2. *Case 2: Gradual Interface:*

The second configuration we consider is a layer with increasing liquid water volume content. To model this, we assume that the dielectric transition at the eutectic behaves as a graded index medium with the dielectric permittivity increasing linearly as a function of range. To calculate the effective reflectivity in this scenario, we used the electromagnetic transfer matrix method (e.g., Born and Wolf, 1970; Grima et al., 2014), which solves Maxwell's equations in a one-dimensional geometry via the successive application of continuity and propagation criteria for the electric field. This technique has previously been used in an electromagnetically analogous radar-sounding context to simulate the effects of graded firn density profiles of surface reflections (Grima et al., 2014).

The model domain is considered a linearly increasing permittivity profile, $\varepsilon(z)$, embedded between two semi-infinite dielectric half-spaces; the "entrance" and "exit" media (Fig. 1). The vertical permittivity gradient, $\frac{\delta\varepsilon}{\delta z}$, was used as a parametric degree of freedom. The permittivity profile was approximated by subdividing the model domain into small slices of constant and increasing permittivity with ice depth, with the discretization interval set at 0.01 m. Physically two different model scenarios can occur, dependent upon the "transition distance" relative to the vertical range resolution (i.e., the distance that it takes for the permittivity to change from ice to liquid complex permittivity (ε_i to ε_l), relative to the scale at which changes in permittivity result in reflection). First, for the case where the transition distance is less than the range resolution, the entrance medium is defined to be ε_i and the exit medium is defined to be ε_l. Second, for the case where the transition distance is greater than the range resolution, the entrance medium is defined to be ε_i and the exit medium is defined to be $\varepsilon_f < \varepsilon_l$. In the first scenario, the thickness of the model domain was set to the transition distance. In the second scenario, the thickness of the model domain was set to the range resolution (15 m and 150 m for the 9 MHz/HF and 60 MHz/VHF systems respectively) following nominal REASON parameters (Blankenship et al., 2009; Grima et al., 2014). Finally, following Mouginot et al. (2009) and Grima et al. (2014) the effects of finite bandwidth (i.e., pulse compression, via a linearly modulated chirp) were incorporated by assuming that the power reflectivity is given by

$$\left[\frac{\Gamma}{\Gamma_o}\right]_{dB} = 10\log_{10}\left(\max(|IFFT|S(f)\rho(f)S^*(f)|^2)\right), \quad (5)$$

where $S(f)$ is the chirp power spectrum, $\rho(f)$ is the complex (E-field) reflectivity as a function of frequency, f is the frequency, and IFFT notates inverse fast Fourier transform. We use $[\cdot]_{dB}$ to denote $10\log_{10}(\cdot)$ and * to denote a complex conjugate.

2.3. Case 3: Liquid Water Pores:

The final configuration we consider is a layer with liquid water pores. We compare the reflectivity and backscatter from a half-space of dielectric spheres (Eluszkiewicz, 2004; Aglyamov et al., 2017) under various mixing formulas and coherent analytic solutions. The size of the spherical water particles considered in this work are small enough compared to the wavelength so that low-frequency approximations of many coherent multiple scattering solutions are applicable. We compare Induced Polarization (Tsang et al., 1985, Chap. 6, Sec. 6.5), Quasi-Crystalline Approximation (Tsang et al., 1985, Chap 6, Sec. 9.2), Polder and van Santen Mixing (Tsang and Kong, 2004, Chap 4, Sec. 3.2), Bilocal (Tsang and Kong, 2004, Chap. 4, Sec. 3.5), and Rayleigh Scattering Approximation (Ulaby and Long, 2014, eq. 8.76, pg 354) models. We use this selection of models because a) they are expressly formulated for scattering from a half-space of small dielectric spheres, b) are analytic, c) are relatively accessible, and d) allow us to compare the results across a variety of scattering assumptions.

2.3.1. Induced Polarization, Rayleigh

The effective wavenumber for a half-space of dielectric spheres derived in the low-frequency limit of induced dipoles (i.e., Rayleigh Scattering Approximation) is (Tsang et al., 1985, Chap. 6, Sec. 6.5),

$$K^2 = k^2 + 3\phi k^2 B \left[1 + i\frac{2}{3}k^3 a^3 BC\right] \tag{6}$$

$$y = \frac{\varepsilon_s - \varepsilon_r}{\varepsilon_s + 2\varepsilon_r} \tag{7}$$

$$B = \frac{y}{1 - \phi y} \tag{8}$$

$$C = \frac{(1-\phi)^4}{(1+2\phi)^2} \tag{9}$$

where ε_s is the dielectric permittivity of the spheres (liquid) with radius a, and ε_r is the dielectric of the background (ice) with wavenumber, $k = \frac{2\pi}{\lambda}$. Given N_v scatterers per unit volume, the liquid porosity is $\phi = N_v v_o$, where $v_o = 4/3\pi a^3$ is the volume of one sphere.

This formulation is coherent and assumes the spheres are distributed according to the Percus-Yevick pair-distribution function. Equation (6) is the same result obtained in the low frequency limit of the Ewald-Oseen Extinction Theorem (EOExT) and the Quasi-Crystalline Approximation (QCA), which we describe and analyze below.

The normalized backscatter cross section (i.e., dimension of 1/Area) for the incoherent scattering component at normal incidence is given by (Tsang et al., 1985, Chap. 6, Sec. 2.3, 7.5)

$$\sigma_{o,vv} = \sigma_{o,hh} = \frac{1}{2\pi n_o}\left|(K-k)k\right|^2 \frac{C}{Im(K)} \tag{10}$$

where $\sigma_{o,vv}$ has units of [m^{-2}], K is set by (6) and Im means imaginary part.

2.3.2. QCA - Coherent Potential

The effective wavenumber of a half-space of dielectric spheres under the Quasi-Crystalline Approximation with Coherent Potential is found by solving the following nonlinear equation for K (Tsang et al., 1985, Chap 6, Sec. 9.2)

$$K^2 = k^2 + \frac{\phi(k_s^2 - k^2)}{1 + \frac{(k_s^2 - k^2)}{3K}(1-\phi)} \left[1 + i \frac{2(k_s^2 - k^2) K a^3 C}{9 \left[1 + \frac{(k_s^2 - k^2)}{3K}(1-\phi) \right]} \right] \quad (11)$$

where $k_s = k\sqrt{\varepsilon_s}$ is the wavenumber in the sphere. This can be written as a 6^{th} order polynomial in K as

$$\sum_{j=0}^{6} a_j K^j = 0 \quad (12)$$

where

$$a_{6,\ldots,0} = [-1,\ iA_2A_4,\ A_1 + A_2 - 2A_3,\ 0,\ 2A_1A_3 + A_2A_3 - A_3^2,\ 0,\ A_1A_3^2], \quad (13)$$

$$A_{1,\ldots,4} = [k^2,\ (k_s^2 - k^2)f,\ (1/3)(k_s^2 - k^2)(1-f),\ (2/9)(k_s^2 - k^2)a^3C], \quad (14)$$

and C is given by (9).

The correct solution is the one root with both positive real and positive imaginary parts, computed with any root finding algorithm. This formulation is the most accurate of those included here and is valid up to $\phi \approx 0.4$.

2.3.3. Polder and van Santen Mixing Formula

The Polder and van Santen mixing formula for m species of dielectric in the low-frequency limit is (Tsang and Kong, 2004, Chap 4, Sec. 3.2)

$$\sum_{p=1}^{m} \frac{\varepsilon_p - \varepsilon_o}{\varepsilon_p - 2\varepsilon_g} \phi_p = \frac{\varepsilon_g - \varepsilon_o}{3\varepsilon_g} \quad (15)$$

$$\sum_{p=1}^{m} \phi_m = 1 \quad (16)$$

where ε_g is the effective permittivity of the medium which must be solved for and ϕ_m is the liquid porosity for species m. Using $m = 2$, background dielectric of ε_r at a certain solid volume fraction, $1-\phi$, and spherical inclusions of dielectric of ε_s at a certain liquid porosity ϕ, eq. (15) becomes

$$\frac{\varepsilon_r - 1}{\varepsilon_r - 2\varepsilon_g}(1-\phi) + \frac{\varepsilon_s - 1}{\varepsilon_s - 2\varepsilon_g}\phi = \frac{\varepsilon_g - 1}{3\varepsilon_g} \tag{17}$$

Arranged as a cubic in ε_g this is

$$a_3\varepsilon_g^3 + a_2\varepsilon_g^2 + a_1\varepsilon_g + a_0 = 0 \tag{18}$$

where $a_{3,\ldots,0} = [4, 2\varepsilon_s - 4\varepsilon_r + 6\varepsilon_r\phi - 6\varepsilon_s\phi + 2, \varepsilon_s - 2\varepsilon_r - 2\varepsilon_r\varepsilon_s + 3\varepsilon_r\phi - 3\varepsilon_s\phi, -\varepsilon_r\varepsilon_s]$. As before, the correct solution is the one root that has both positive real and positive imaginary parts. The effective permittivity, ε_{eff}, is used in eq. (2) to compute the reflectivity of the layer.

2.3.4. Bilocal Approximation

The bilocal approximation is a second-order coherent scattering solution under the assumption of weak scattering. The effective permittivity for spherical inclusions is given by (Tsang and Kong, 2004, Chap. 4, Sec. 3.5),

$$\varepsilon_{eff} = \varepsilon_g \left[1 + i2k_g^3 a^3(\phi y_s^2 + (1-\phi)y_b^2)\right] \tag{19}$$

$$y_s = \frac{\varepsilon_s - \varepsilon_g}{\varepsilon_s + 2\varepsilon_g} \tag{20}$$

$$y_b = \frac{\varepsilon_r - \varepsilon_g}{\varepsilon_r + 2\varepsilon_g} \tag{21}$$

where ε_g is computed from (15). This formulation includes scattering loss (the imaginary part of (19)), which is not captured by the mixing formula (15). The normalized backscatter cross section for the incoherent component at normal incidence under the bilocal approximation is (Tsang and Kong, 2004, Chap 4, Sec. 3.5)

$$\sigma_{o,vv} = \sigma_{o,hh} = 3|k_g|^4 a^3 \left[(\phi|y_s|^2 + (1-\phi)|y_b|^2)\right] \frac{|k|^2}{|K|^2} |X_{01}X_{10}|^2 \frac{1}{4Im(K)} \quad (22)$$

where $K = k\sqrt{\varepsilon_{eff}}$ and X are the effective transmission coefficients

$$X_{01} = \frac{2\sqrt{\varepsilon_{eff}}}{\sqrt{\varepsilon_{eff}} + \sqrt{\varepsilon_r}} \quad (23)$$

$$X_{10} = \frac{2\sqrt{\varepsilon_r}}{\sqrt{\varepsilon_{eff}} + \sqrt{\varepsilon_r}} \quad (24)$$

2.3.5. Rayleigh Scattering Approximation

Here we look at scattering of the half-space under the Rayleigh Approximation. The volumetric incoherent backscatter from a collection of spheres under the Rayleigh Scattering Approximation is

$$\sigma_V = 4\pi|k|^4|y|^2 \sum_{j=1}^{N_v} r_j^6 \quad (25)$$

where σ_V has units of [m^{-1}], N_v is the number of particles with radius r_i per given volume [m^3], and y is given by eq. (7) (Ulaby and Long, 2014, eq. 8.76, pg 354). For identical particles this becomes

$$\sigma_V = 3|k|^4|y|^2 N_v v_o a^3 \quad (26)$$

where v_o is the volume of a single sphere. Therefore, we obtain the liquid porosity through $N_v v_o = \phi$. Simplifying eq. (26) gives

$$\sigma_V = 3|k|^4|y|^2 \phi a^3 \quad (27)$$

The radar equation for a target described by the normalized radar cross section is:

$$\sigma = \oint_V \sigma_V dV \quad (28)$$

We assume the radar scattering is uniform over the volume hence eq. (28) simplifies to $\sigma = \sigma_V V$ [m^2]. The unitless area-normalized backscatter, $\sigma_o = \sigma_V V/A$ is then

$$\sigma_o = 3|k|^4 a^3 |y|^2 \phi \frac{V}{A}. \tag{29}$$

Both the area and volume must describe the region that is the intersection of the leading edge volume and the eutectic zone. The general form of the surface area, A, of the imaged region as described by a surface around the imaged volume (spherical segment) is $A = 2\pi \int r\sqrt{1+\frac{dr}{dz}}dz$, where $r = \sqrt{R_l^2 - z^2}$ is the radial distance from the z axis. The z axis runs normal to the moon's surface (Fig. 2a). Integrating this from either R (the distance from the radar to the trailing edge of the echo) or d (the distance from the radar to the eutectic) to the leading edge of the echo, R_l, gives the pulse-limited area: $A = 2\pi T R_l$, where T is the thickness of the imaged layers.

We derive a general form of the sampled volume, V, however the solution condenses with specific simplifications,

$$\begin{aligned} V =& \int_d^{d+T} \pi((R+\chi)^2 + y^2)dy - \int_d^{d+T_s} \pi(R^2 + y^2)dy \\ V =& \pi T\left[(R+\chi)^2 - (R+\chi-T)^2 - T(R+\chi-T) - \frac{1}{3}T^2\right] \\ & - \pi T_s(R^2 - d^2 - T_s d - \frac{1}{3}T_s^2) \end{aligned} \tag{30}$$

where T_s is the distance between the top of the sampled region to the trailing edge of the echo. For simplicity, we assume the leading edge volume is a spherical cap as illustrated in Figure 2b, hence we take $T = \chi$ and $R_l = d + \chi$. The range resolution of the radar system is $\chi = \frac{2c}{\beta n}$, where c is the speed of light and β is bandwidth. With these simplifications, the sampled volume is then,

$$V = \frac{1}{6}\pi\chi^2(6d + 4\chi). \tag{31}$$

Plugging in A and V gives,

$$\sigma_o = 3|k|^4 a^3 |y|^2 \phi \frac{\frac{1}{6}\pi\chi^2(6d+4\chi)}{2\pi\chi(d+\chi)} \tag{32}$$

$$= |k|^4 a^3 |y|^2 \phi \frac{\chi(3d+2\chi)}{2(d+\chi)} \tag{33}$$

2.3.6. Coherent and Incoherent Effective Reflectivities

In order to determine the coherent and incoherent effective reflectivities at the interface of a liquid pore rich layer, we model a system that uses QCA with Coherent Potential (QCA-CP) and Rayleigh Scattering Approximation for the coherent and incoherent components, respectively. Of the tested models, QCA-CP is the most accurate for a coherent measurement and we use the Rayleigh Scatting Approximation for the incoherent measurement of the scattering layer.

We define the received power from the coherent component to be given by the radar equation derived under the the image method over a flat interface (Peters et al., 2005; Haynes et al., 2018),

$$P_r = \frac{P_t G_t G_r \Gamma \lambda^2}{2^6 \pi^2 R^2} \tag{34}$$

At the interface, normalized coherent component is then the coherent component, eq. (34) normalized by the baseline, Fresnel reflection ($P_{\text{coh},100\%}$, eq. (34) evaluated with the reflectivity of the ice-water interface).

$$\frac{P_{\text{coh}}}{P_{\text{coh},100\%}} = \frac{\Gamma_{\text{coh}}}{\Gamma_o}. \tag{35}$$

We substitute the effective power reflection coefficient for a coherent reflection, Γ_{coh}, and Fresnel reflection, Γ_o as defined by eq. (2),

$$\frac{P_{\text{coh}}}{P_{\text{coh},100\%}} = \frac{\left|\frac{K-k}{K+k}\right|^2}{\Gamma_o} \tag{36}$$

where K is the effective wavenumber for a half-space of dielectric spheres under the QCA-CP as given by eq. (11).

The normalized backscatter radar equation is

$$P_{\text{coh}} = \frac{P_t G_t G_r \lambda^2 \sigma_o A}{(4\pi)^3 R^4}. \tag{37}$$

Normalizing it by the baseline coherent power, $P_{\text{coh},100\%}$, eq. (34) reduces to

$$\frac{P_{\text{incoh}}}{P_{\text{coh},100\%}} = \frac{\sigma_o A}{\pi R^2 \Gamma_o} \tag{38}$$

We use eq. (33) and the range to the eutectic ($R = d$) to get the effective incoherent reflectivity for spherical pores,

$$\frac{P(R, r, \phi, V)}{P_{\text{coh},100\%}} = \frac{1}{2}\frac{|k|^4 a^3 \phi \chi^2 (6d + 4\chi)}{d^2}\left|\frac{y}{\Gamma_o}\right|^2. \tag{39}$$

The Rayleigh Approximation does not hold for $ka > 0.7$ (Ulaby and Long, 2014, Fig. 8–21). Therefore, we test different ranges and radii for $ka = 0.005$ and $ka = 0.14$. The radii for low ka are $a = 2.7,\ 4.0$ cm for HF and VHF, respectively. The radii for high ka are $a = 79,\ 12$ cm for HF and VHF, respectively. We test ranges of 25 and 100 km. We also test a constant radius and range with different REASON frequencies.

3. Results

We find that the power return is the greatest for a layer of fully liquid water, which is the baseline case used in most link budgets. A sharp-interface between ice and a two-phase mixture of ice and water (Case 1), a layer with increasing liquid porosity (Case 2), and a layer with liquid water pores (Case 3) all fall along the spectrum between an undetectably weak return and the return from a specular layer of liquid water. Our results suggest that for each of the three configurations, there is a range of geophysical and observational parameters for which radar returns would be produced that are within a detectable range for radar sounders (e.g., effective reflectivity values of ≥ -70, -30, or -10 dB (Kalousová et al., 2017)). Though, of course, the exact effective reflectivity values of each configuration will vary with porosity and porosity gradient.

3.1. Case 1: Sharp Interface

For a sharp interface between ice and a two-phase mixture of ice and water, it follows from eq. (1) and eq. (3) that the reflectivity can be modelled as a function of ϕ. Figure 3 shows these relationships for fresh, saline and brine water using the complex permittivities in eq. (4). For all water, the reflectivity increases as a function of ϕ, with reflectivity ~ 2.5 dB greater for saline water and reflectivity ~ 2 dB less for brine water when $\phi = 1$ (Fig. 3). For salty water, echo strength and detectability increases by as much as 20 dB from the fresh water approximation. For brine water, the difference in permittivity of the liquid water would reduce the echo strength and detectability by as much as 10 dB from the fresh water approximation and 30 dB from the salt water approximation. However, this effect will be partially offset by the increase in conductivity depending on the details of the contaminant and its concentration. In the rest of this study we focus on the reduction in reflectivity from the baseline case of fresh water.

3.2. Case 2: Gradual Interface

In this case, the liquid water content gradient determines relative reflectivity. At high liquid water content gradients, the HF and VHF behave similarly. At lower porosity gradients, the HF and VHF begin to deviate in magnitude of relative reflection. The HF band performs better than the VHF band because the HF band samples a larger thickness (due to a coarser range resolution), resulting in a larger difference in permittivity. A positive relationship occurs between the permittivity gradient, $\frac{\delta \varepsilon}{\delta z}$, and effective reflectivity, Γ (Fig. 4). For a given $\frac{\delta \varepsilon}{\delta z}$, Γ from the 9 MHz/HF radar is always greater than for the 60 MHz/VHF radar. Conceptually, this difference arises due to the greater wavelength, therefore coarser vertical resolution, of the HF radar. For the same gradient of permittivity, the permittivity increases more per wavelength for the HF than the VHF.

The high permittivity gradient limit (right hand side of Fig. 4) corresponds to the case of a specular Fresnel reflection. Prior analytical work by Simpson (1976), (consistent with Fig. 4) demonstrates that refection from the graded index range cell can be well approximated by the specular result for transition distances below ~ 20 % of the incident wavelength. For the 9 MHz/HF system (wavelength ~ 18.8 m in ice), the "specular regime" (e.g., Schroeder et al., 2015), therefore, corresponds to a transition distance < 3.8 m (permittivity gradient $> 20\ \mathrm{m}^{-1}$), while for the 60 MHz/VHF system (wavelength ~ 2.8 in ice), the specular regime, corresponds to a transition distance < 0.56 m (permittivity gradient $> 140\ \mathrm{m}^{-1}$).

The low permittivity gradient limit (left hand side of the graph) corresponds to an approximately linear relationship between $[\Gamma]_{dB}$ and $\log_{10}\left(\frac{\delta\varepsilon}{\delta z}\right)$. We can gain a better analytical understanding of this relationship by assuming that

$$\Gamma \equiv |\rho|^2 \propto \delta\varepsilon^{2,} \tag{40}$$

where $\delta\varepsilon$ is the change in real part of permittivity associated with the reflection. The scaling relationship, (40), is motivated by the $\delta\varepsilon$ dependence of the Fresnel equation for small permittivity contrasts given by Paren and Robin (1975) where $|\rho|^2 = \left(\frac{\delta\varepsilon}{4\bar{\varepsilon}}\right)^2$ and $\bar{\varepsilon}$ is the mean permittivity. Here, we assume proportionality rather than equality because Paren and Robin, 1975 is only valud for sharp interfaces. Expressing (40) in dB units gives

$$[\frac{\Gamma}{\Gamma_o}]_{dB} \propto 20\log_{10}(\delta\varepsilon). \tag{41}$$

Finally, via the linearity of $\left(\frac{\delta\varepsilon}{\delta z}\right)$, it follows that

$$\frac{\delta[\Gamma]_{dB}}{\delta(\log_{10}\left(\frac{\delta\varepsilon}{\delta z}\right))} = 20\ \mathrm{dB} \tag{42}$$

which is in good agreement with low permittivity gradient regime in Fig. 4. For example, if a linear approximation is assumed to fit the data over $\left(\frac{\delta\varepsilon}{\delta z}\right) = 10^{-2}$ m^{-1} to $\left(\frac{\delta\varepsilon}{\delta z}\right) = 10^{-1}$ m^{-1} then the simulated gradients are within 2% of eq. 42.

3.3. Case 3: Liquid Water Pores

We compare the coherent relative reflectivity and the incoherent normalized backscatter at normal incidence using HF (Fig. 5) and VHF (Fig. 6) (Bruzzone et al., 2013; Blankenship et al., 2009). These figures show that the Rayleigh Scattering Approximation results in the highest predicted incoherent energy for all liquid porosity at HF and most (> 0.3) liquid porosity at VHF. However, they also show that for liquid porosity > 0.2, coherently reflected energy dominate incoherent energy by orders of magnitude in the radar return. In order to determine whether the eutectic zone will be detected, we look at the reflection off of the eutectic interface using both the coherent relative reflectivity and incoherent normalized backscatter as modeled by QCA-CP and Rayleigh Scattering Approximation, respectively,

$$\frac{P_{\text{absolute}}}{P_{\text{coh,100\%}}} = \frac{P_{\text{coh}} + P_{incoh}}{P_{\text{coh,100\%}}}. \quad (43)$$

We assume that the combination of QCA-CP and the Rayleigh Scatter Approximation (as plotted in Fig. 7) will provide the most valid total echo strength up to $\phi \approx 0.4$ (Tsang and Kong, 2004; Saulnier et al., 1990). Additionally, this combination provides a conservative lower-bound on the total echo strength for higher porosity (Fig. 5C and 6C).

At the interface of ice and a layer composed of spherical scattering liquid water bodies, the return signal depends most sensitively on liquid porosity (Fig. 7). The coherent reflected energy dominates over the incoherent energy, therefore the reflection is mostly independent of liquid pore radii (Fig. 8), and the range from radar to eutectic depth (Fig. 7).

At the low porosity limit, the size of the pores alters the effective reflectivity. In HF and VHF (Fig. 7a), larger liquid pores, which correspond to higher ka values, are easier to detect. VHF (Fig. 7b) shows greater sensitivity to pore size for smaller ka values. At low porosity ($< 10^{-3}$), effective reflectivity at VHF for low ka begin to diverge from one another.

Compared to HF, the VHF, $ka = 0.14$ curve has lower effective reflectivity at low porosity values.

4. Discussion

Although the combined effect of ice shell processes, chemical composition, thermal structure and ice shell thickness determine eutectic zone properties, here we focus on which liquid water parameters in the end-member cases govern the detection ability at the eutectic isotherm. Following Kalousová et al. (2017), we discuss three detectability thresholds relative to the specular water layer to explore: 70 dB, 30 dB, and 10 dB (excess power available to compensate for modeled attenuation, surface losses, and radar parameters).

4.1. Case 1: Sharp Interface

Our results show that at the limit when the porosity approaches 0, the permittivity of the layer reaches ice permittivity. With 70 dB, 30 dB, and 10 dB excess power at the liquid filled layer, the ice penetrating radar sounder would detect layers with porosity greater than 4×10^{-4}, 0.04 and 0.5, respectively (Fig. 3).

4.2. Case 2: Gradual Interface

The results from the gradual interface show that the different radar frequencies perform differently at the interface of a layer with increasing liquid water content and pure solid ice. The higher frequency sounder has a shorter wavelength and wider bandwidth and, therefore, samples a smaller dielectric transition than does lower frequency sounder. As a result, the interface using the VHF sounder produces a smaller signal, weaker reflection, than the HF sounder. As an example, if excess return power is 70 dB then the HF would be able to detect all tested porosity gradients, $\geq 10^{-4}$ m^{-1}. If the excess return power is 30 dB, the HF would be able to detect $\geq 3 \times 10^{-3}$ m^{-1} whereas the VHF would only be able to detect $\geq 2 \times 10^{-2}$ m^{-1}. If the excess return power is 10 dB, the HF would be able to detect $\geq 10^{-2}$ m^{-1} whereas the VHF would only be able to detect $\geq 3 \times 10^{-1}$ m^{-1}.

The effective reflectivity is different for the HF and VHF at low porosity gradients. Since the sharp interface (Case 1) does not have a frequency dependence, the resulting effective reflectivitiy from both frequencies would be the same. The difference in relative reflection power of HF and VHF, which is absent in the sharp interface case (Case 1), could potentially be exploited to determine whether a subsurface interface has a sharp interface with a specific porosity and certain composition or a gradual interface with a certain composition.

4.3. Case 3: Liquid Water Pores

Relative to Fresnel reflection, a layer with liquid water pores may go undetected if the porosity of the layer of pores is too low (Fig. 7). HF has slightly higher effective reflectivities than VHF, because of the dominant coherent reflection. Of the tested excess powers, 70 dB would be able to detect all of the tested cases above 10^{-3} vol% using both HF and VHF. Using HF with 30 dB and 10 dB excess power, liquid porosity greater than 3.5×10^{-2} and 0.18 would be detected, respectively. If the pore radii are 79 cm or greater, then with 30 dB, liquid porosity greater than 2.0×10^{-2} would be detected. Using VHF, with 30 dB and 10 dB, liquid porosity greater than 3×10^{-2} and 0.18 would be detected, respectively.

Since the results for HF and VHF are different (Fig. 7), there is a potential to use these bands together to speculate on parameter inversions (Fig. 8). However, this would require a detailed analysis of the non-uniqueness of the problem and noise from the nearby features to be able to state whether this is feasible. Therefore, we leave this investigation as possible future research.

4.4. Cross-Case Synthesis

Taken as a whole, the results in this paper suggest that water in the eutectic zone could provide a detectable target for radar sounding with effective reflectivity values greater than -50 dB across a wide range of parameters and all three end-member cases we explored. Given the much lower attenuation values for eutectic reflections (compared to ice ocean reflections) (Kalousová et al., 2017), this makes the eutectic zone an appealing target to add to radar sounding mission to explore the shells of icy moons. The ability to detect the eutectic zone of the Europan ice shell would provide greater insight into ice-shell processes. For example, spatial variations in the eutectic zone could result from heterogeneities in the ice shell (Thomson and Delaney, 2001; Culha and Manga, 2016), convection in the shell (e.g., Kalousová et al., 2017; McKinnon, 1999), or other physical processes that might be linked to the observed surface features (Collins et al., 2000; Dombard et al., 2013; Michaut and Manga, 2014) or ice shell dynamics, thickness, and thermophysical properties (e.g., Spaun and Head, 2001; Kargel, 2000; Greenberg et al., 2000; Prieto-Ballesteros and Kargel, 2005).

While there are other plausible configuration for water in eutectic zone of Europa's ice shell, we believe that the end-member models presented in this paper will bound the detectability of many of those geometries as well. For example, some models suggest that the lenticulae on Europa's surface formed through water injections in to the ice shell in the form of sills (e.g., Michaut and Manga, 2014). If the cross sectional area of the crack normal to the radar sounder is larger than the Fresnel area, then the radar sounder would resemble signal strengths of Case 1. If the cross sectional area is less than the Fresnel area, it may go undetected. If there are multiple cracks at considerable volume density, then the radar signal might scatter producing a signal (Case 3). Although the Rayleigh Scattering Approximation was used for Case 3, which required a radius less than a critical value, cracks larger than the critical radius will result in even greater scattering and hence a stronger signal.

The analysis presented here is not meant to provide a complete echo strength values for realistic eutectic and ice shell configurations at Europa. More sophisticated and complete analysis will have to be undertaken in follow-on studies when actual instrument parameters and observations are available. Instead, we seek simple models to make the case that water in Europa's eutectic zone is a plausible target for radar sounding detection and that it, along with shallow water lenses and the ice-ocean interface, should be included in such follow-on studies.

5. Conclusion

One of the primary targets for the radar sounding instruments on NASA's and ESA's missions to Europa is liquid subsurface water in shallow lenses or at the ice/ocean interface. Our analysis suggest that bodies of liquid water in the eutectic zone could be detected by radar sounding. We analyze three different possible configurations water at the eutectic to evaluate the effective reflectivity and, therefore, detectability of these bodies. The first configuration is a specular interface of a mixture of water and ice. Both the HF and VHF perform equally at this interface. The second configuration is a layer with increasing water porosity. Sharper gradients in liquid water content produce higher relative reflection than smaller gradients. The HF band produces higher effective reflectivity values than the VHF because a given porosity gradient changes more over the longer wavelength scale. The last configuration is a layer with scattering liquid pores. The effective reflectivity is mainly dependent on porosity. We find that, for each configuration, a range of physically plausible eutectic parameters exist that could produce detectable echoes, with effective reflectivity values greater than -50 dB at HF or VHF frequencies. Imaging liquid water, especially the eutectic zone, will reveal fundamental information on ice shell processes, thermal profile, chemical structure, and ice shell characteristics at Europa.

6. Acknowledgements

The authors would like to acknowledge the reviewers, Francis Nimmo, Don Blankenship, David Stillman, and the Measurement Implement Groups from the REASON Science Team for their technical discussions and valuable conversations. C.C was supported, in part, by NSF-GRFP and Lieberman Fellowship at Stanford University. A portion of this work was carried out by the Jet Propulsion Laboratory, California Institute of Technology, under a contract with the National Aeronautics and Space Administration.

7. Variable Table

variable	significance	variable	significance
P_r	received power	K	effective wavenumber
Γ_o	Fresnel power reflection	k_s	wavenumber of the sphere
ε	complex permittivity, dielectric	$S(f)$	chirp power spectrum
ε_o	free space permittivity	$\rho(f)$	complex (E-field) reflectivity
$\bar{\varepsilon}$	mean permittivity	r	radius
ε_f	exit ε	a	sphere radius (Case 3)
ε_r	background ε	N_v	NO of scatterers per unit vol.
ε_s	effective ε of sphere	$v_o = \frac{4\pi a^3}{3}$	sphere volume
ε_l	liquid ε	z	depth from radar
ε_i	ice ε	ϕ	liq. porosity/ volume fraction
ε_{eff}	effective ε	ϕ_m	m specie porosity
ε_g	effective ε used in PvS	X	effective transmission coef.
$\varepsilon_{l,f}$	fresh liquid water ε	α	dimensionless param. (mixing)
$\varepsilon_{l,s}$	saline liquid water ε	A	SA normal to radar sounder
$\varepsilon_{l,b}$	brine liquid water ε	T	thickness of the eutectic zone
$\frac{\delta\varepsilon}{\delta z}$	vertical ε gradient	T_s	thickness of the excess vol.
σ	backscattering cross section	d	range to eutectic
$\sigma_{o,vv/hh}$	transmit/receive V/H polarization	R	radar to the target range
σ_V	volumetric incoherent σ	R_l	radar to leading range
f	frequency	V	imaged vol. of eutectic zone
χ	range resolution	$IFFT$	inverse fast Fourier transform
c	speed of light	$[\cdot]_{dB}$	$10\log_{10}(\cdot)$
τ	one-way path attenuation	$*$	complex conjugate
n	complex index of refraction	$Im(\cdot)$	imaginary part
λ	wavelength	$i = \sqrt{-1}$	imaginary number
$k = \frac{2\pi}{\lambda}$	wavenumber		

Table 1: SA=surface area, coef.=coefficient, liq. = liquid, vol. = volume, NO = number

421 ## 8. Figures

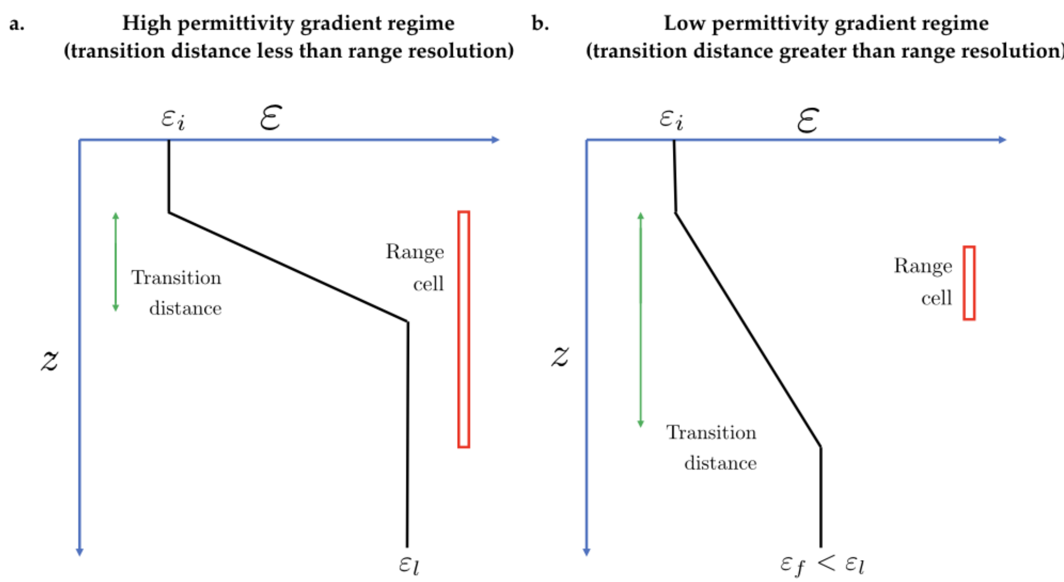

Figure 1: Transfer matrix simulation domains for graded permittivity structure (layer with increasing water volume density). Two different model boundary conditions are used for the exit medium dependent upon the size of the transition distance relative to the range resolution.

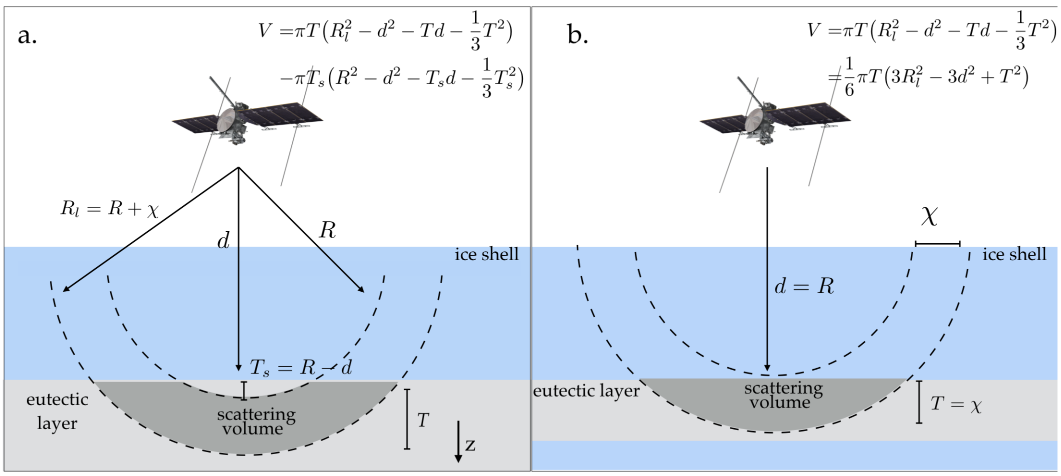

Figure 2: **Scattering volume calculation:** We provide a general description of the intersection of the leading edge volume and the eutectic zone in (a). In our analysis, we simplify the analysis to a spherical cap, which represents the initial interaction between the leading edge volume and the eutectic zone as illustrated in (b). We assume that the range resolution, χ, is the thickness of the measured scattering volume. It is not the thickness of the eutectic zone. R and R_l are the trailing and leading edges of the echo. d is the depth to the eutectic from the radar. T_s is the distance between the top of the eutectic zone and the trailing edge of the echo at the center of the radar. We define z as the axis normal to the moon's surface.

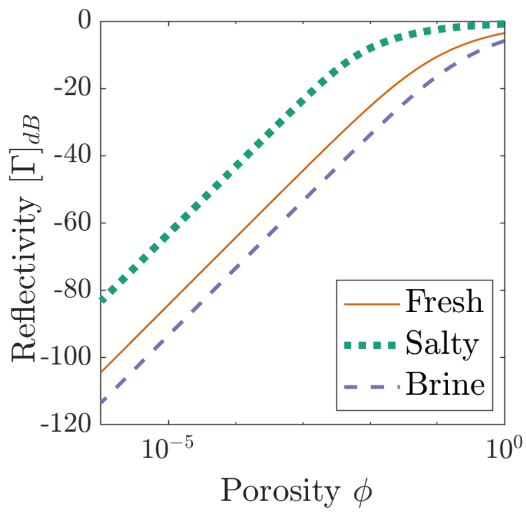

Figure 3: **Reflectivity as a function of porosity for Case 1 with fresh, saline and brine water.** The complex permittivities are given in eq. 4.

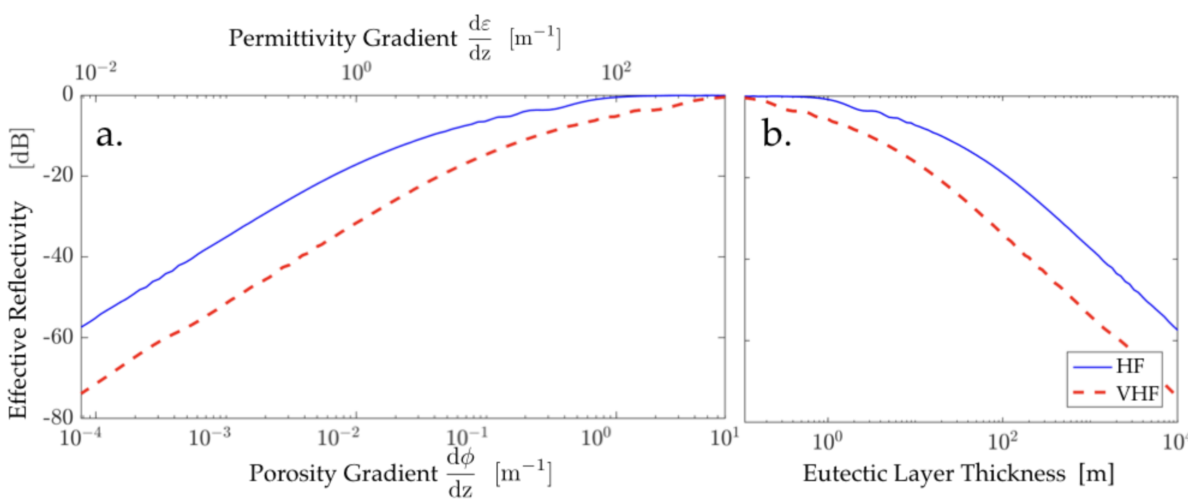

Figure 4: **Effective reflectivity, Γ, versus (a) log permittivity gradient, $\log_{10}\frac{\delta\varepsilon}{\delta z}$, log porosity gradient, $\log_{10}\frac{\delta\phi}{\delta z}$, and (b) the eutectic layer thickness, given a transition from 0 to 1.0 liquid porosity.**

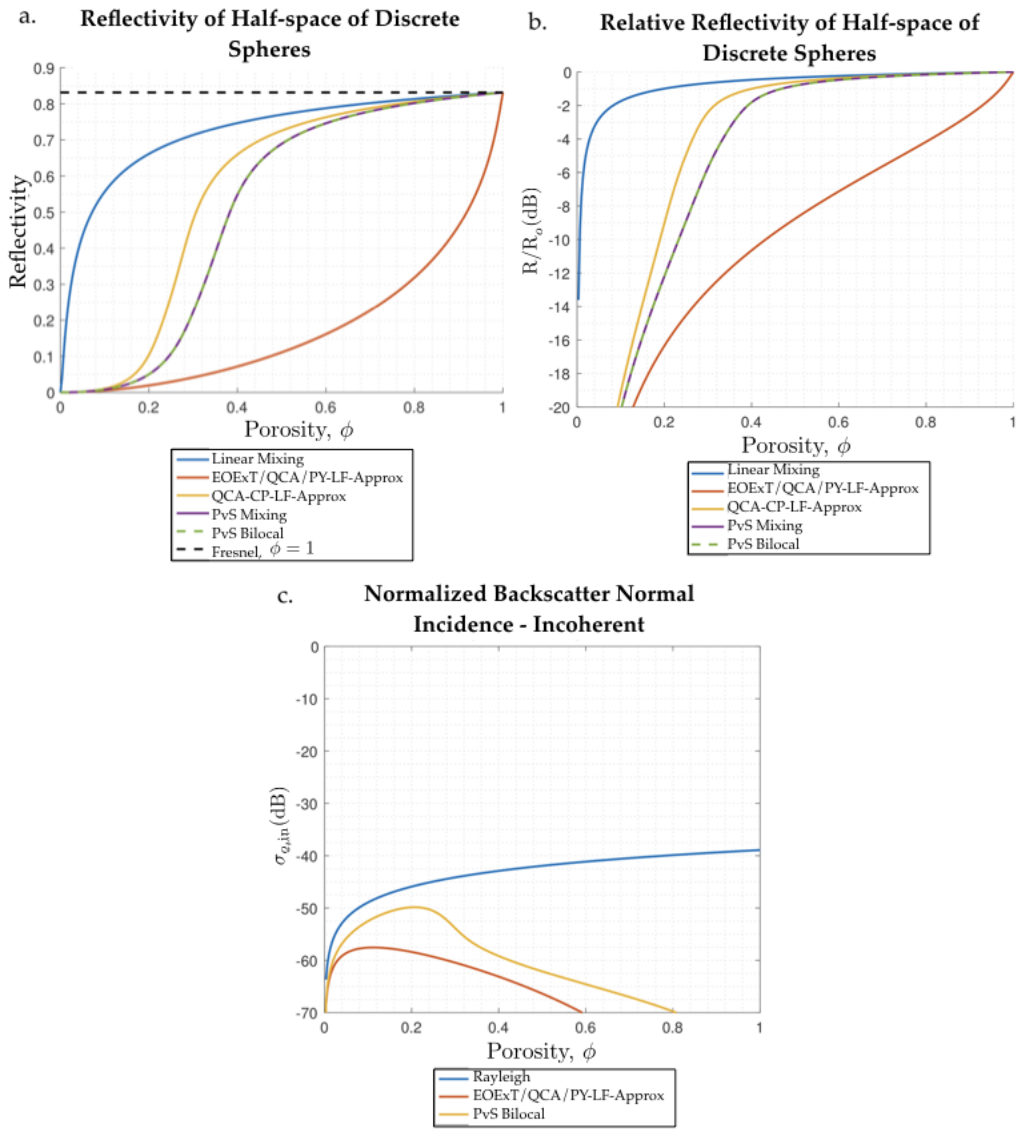

Figure 5: **Reflectivity (a), effective reflectivity (b), and incoherent backscatter (c) for various scattering models at HF.** Reflectivity is computed from the effective wavenumber or dielectric predicted by each model. The effective reflectivity is normalized to the reflectivity for homogeneous water half-space. The values used for these figures are $\varepsilon_r = 3.4 + 0.17i$, $\varepsilon_s = 80 + 904i$, $f = 9$ MHz, $a = 0.026$ m, and ka $= 0.0049$.

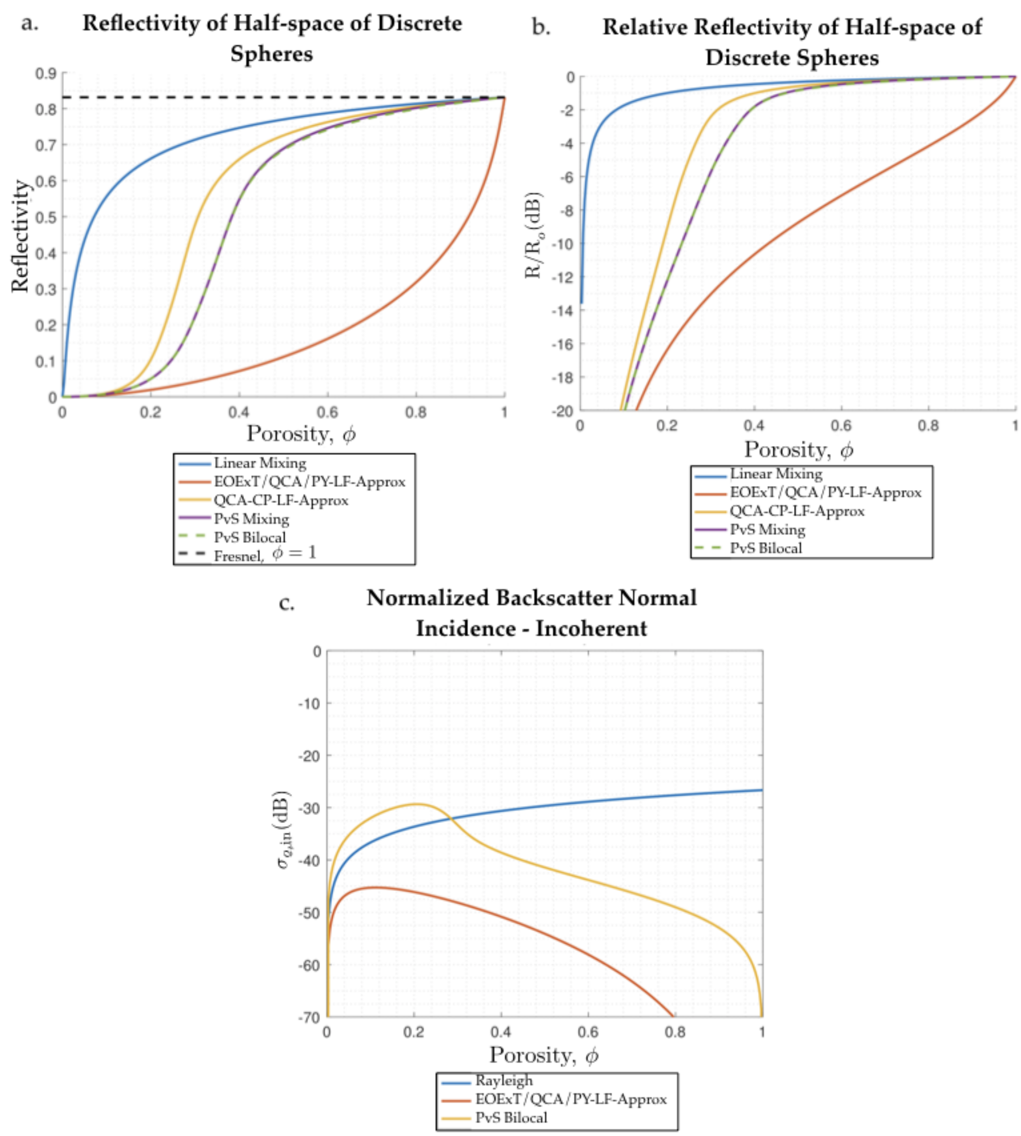

Figure 6: **Reflectivity (a), effective reflectivity (b), and incoherent backscatter (c) for various scattering models at VHF.** Reflectivity is computed from the effective wavenumber or effective dielectric predicted by each model and represents the coherent, specular component of the reflected power. The effective reflectivity is normalized to the reflectivity for homogeneous water half-space. The normalized backscatter is the incoherent scattering component predicted by each model, which is very small in each case due to the small size of the water voids. The values used for these figures are $\varepsilon_r = 3.4 + 0.17i$, $\varepsilon_s = 80 + 904i$, $f = 60$ MHz, $a = 0.01$ m, and ka $= 0.013$.

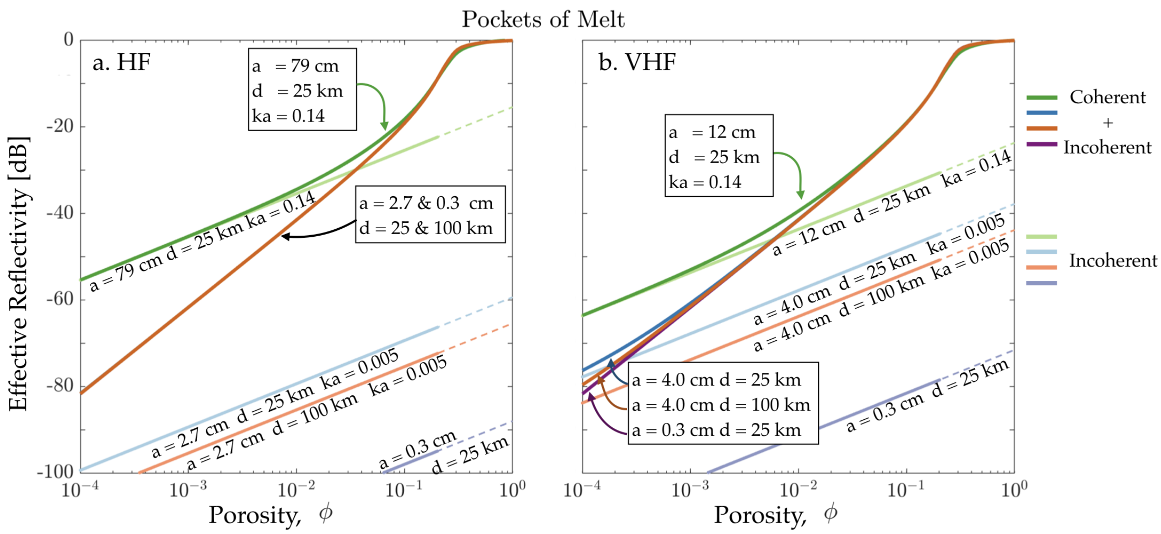

Figure 7: **Effective reflectivity [dB]: Radar echo strength for Case 3 using a. HF radar and b. VHF radar for REASON.** The dark colored lines are the sum of the coherent relative reflectivity and incoherent normalized backscatter components as modeled by QCA-CP and Rayleigh Scattering Approximation, respectively. At the interface, the coherent component dominates. Therefore, except at higher ka values, the result becomes independent of pocket of liquid size and distance from radar to the eutectic. In the eutectic zone, we represent the incoherent scattering using the Rayleigh Approximation. The Rayleigh Scattering provides variable results depending on pore size and range from radar to eutectic depth. Rayleigh Scattering Approximation is shown to fail past liquid porosity of 0.2, therefore we indicate those results using dashed lines.

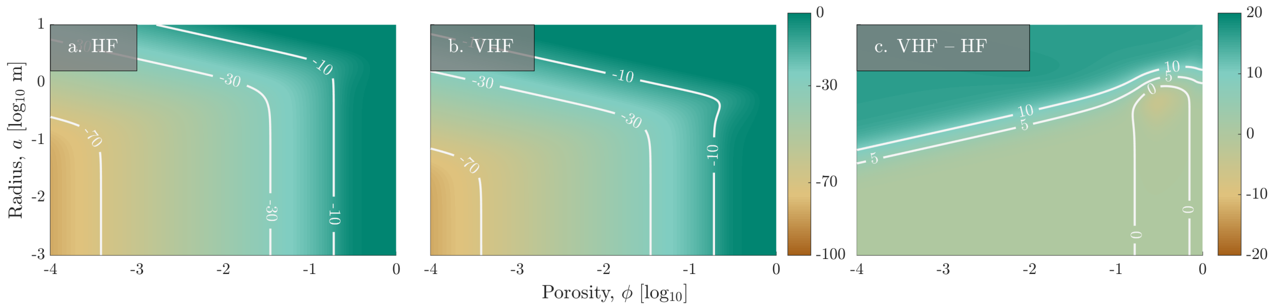

Figure 8: **Effective reflectivity [dB]: Radar echo strength for Case 3 using a. HF radar, b. VHF radar, and c. the difference of HF and VHF for REASON.** The effective reflectivity is modeled by the sum of QCA-CP and Rayleigh Scattering Approximation using variable liquid porosity and liquid pocket radius.

9. References

Y. Aglyamov, D. M. Schroeder, and S. D. Vance. Bright prospects for radar detection of Europas ocean. *Icarus*, 281:334–337, 2017. ISSN 0019-1035. doi: 10.1016/j.icarus.2016.08.014.

D. D. Blankenship, D. A. Young, W. B. Moore, and J. C. Moore. Radar Sounding of Europa's Subsurface Properties and Processes:. *Europa*, 80:631–654, 2009. doi: 10.2307/j.ctt1xp3wdw.33.

M. A. Born and E. Wolf. *Principle of Optics, 4th ed.*, chapter 1. Pergamon Press, Cambridge, 1970.

L. Bruzzone, J. J. Plaut, G. Alberti, D. D. Blankenship, F. Bovolo, B. A. Campbell, A. Ferro, Y. Gim, W. Kofman, G. Komatsu, W. McKinnon, G. Mitri, R. Orosei, G. W. Patterson, D. Plettemeier, and R. Seu. Rime: Radar for icy moon exploration. In *2013 IEEE International Geoscience and Remote Sensing Symposium - IGARSS*, pages 3907–3910, July 2013. doi: 10.1109/IGARSS.2013.6723686.

L. Bruzzone, J. Plaut, G. Alberti, D. Blankenship, F. Bovolo, B. Campbell, D. Castelletti, Y. Gim, A. Ilisei, W. Kofman, G. Komatsu, W. McKinnon, G. Mitri, A. Moussessian, C. Notarnicola, R. Orosei, G. Patterson, E. Pettinelli, and D. Plettemeier. Jupiter icy moon explorer (JUICE): advances in the design of the radar for icy moons (RIME). *Proc. 35th IEEE Int. Geosci. Remote Sens. Symp. (IGARSS 2015)*, pages 1257–1260, 2015.

M. G. P. Cavitte, D. D. Blankenship, D. A. Young, D. M. Schroeder, F. Parrenin, E. Lemeur, J. A. Macgregor, and M. J. Siegert. Deep radiostratigraphy of the East Antarctic plateau: connecting the Dome C and Vostok ice core sites. *Journal of Glaciology*, 62:323–334, 2016. ISSN 0022-1430. doi: 10.1017/jog.2016.11.

G. Collins, J. Head, R. Pappalardo, and N. Spaun. Evaluation of models for the formation on Europa. *J. Geophys. Res.*, 105(E1):1709–1716, 2000.

C. Culha and M. Manga. Geometry and spatial distribution of lenticulae on Europa. *Icarus*, 271:49–56, 2016.

F. Di Paolo, B. Cosciotti, S. E. Lauro, E. Mattei, E. Pettinelli, and G. Vannaroni. Thermal and electromagnetic models for radar sounding of the galilean satellite icy crusts. In *Proceedings of the 15th International Conference on Ground Penetrating Radar*, pages 362–366, June 2014. doi: 10.1109/ICGPR.2014.6970446.

F. Di Paolo, S. E. Lauro, D. Castelletti, G. Mitri, F. Bovolo, B. Cosciotti, E. Mattei, R. Orosei, C. Notarnicola, L. Bruzzone, and E. Pettinelli. Radar signal penetration and horizons detection on Europa through numerical simulations. *IEEE J. Sel. Top. Appl. Earth Obs. Remote Sens.*, 10(1):118–129, 2017.

A. J. Dombard, G. W. Patterson, A. P. Lederer, and L. M. Prockter. Flanking fractures and the formation of double ridges on Europa. *Icarus*, 223 (1):74–81, 2013. ISSN 00191035. doi: 10.1016/j.icarus.2012.11.021. URL `http://dx.doi.org/10.1016/j.icarus.2012.11.021`.

J. Eluszkiewicz. Dim prospects for radar detection of Europa's ocean. *Icarus*, 170(1):234–236, 2004. ISSN 00191035. doi: 10.1016/j.icarus.2004.02.011.

O. Grasset, M. K. Dougherty, A. Coustenis, E. J. Bunce, C. Erd, D. Titov, M. Blanc, A. Coates, P. Drossart, L. N. Fletcher, H. Hussmann, R. Jaumann, N. Krupp, J. P. Lebreton, O. Prieto-Ballesteros, P. Tortora, F. Tosi, and T. Van Hoolst. JUpiter ICy moons Explorer (JUICE): An ESA mission to orbit Ganymede and to characterise the Jupiter system. *Planet. Space Sci.*, 78:1–21, 2013. ISSN 00320633. doi: 10.1016/j.pss.2012.12.002. URL `http://dx.doi.org/10.1016/j.pss.2012.12.002`.

R. Greenberg, P. Geissler, B. R. Tuffs, and V. Hoppa. Habitability of Europa ' s crust : The role of tidal-tectonic processes coupled time variability of orbits and tides was reviewed by. *J. Geophys. Res.*, 105(E7):17551–17562, 2000.

C. Grima, D. Blankenship, D. A. Young, and D. M. Schroeder. Surface slope control on firn density at Thwaites Glacier, West Antarctica: Results from airborne radar sounding. *Geophys. Res. Lett.*, 41:6787–6794, 2014. doi: doi:10.1002/ 2014GL061635.

C. Grima, D. Blankenship, and D. Schroeder. Radar signal propagation through the ionosphere of Europa. *Planet. Space Sci.*, 117:421–428, 2015.

P. Gudmandsen. Electromagnetic probing of ice. *Electromagnetic probing in Geophysics*, 1971. URL `https://ci.nii.ac.jp/naid/10015472911/en/`.

M. S. Haynes, E. Chapin, and D. M. Schroeder. Geometric Power Fall-off in Radar Sounding. *IEEE Geosci. Remote Sens. Lett.*, pages 1–15, 2018.

E. Heggy, E. Palmer, W. Kofmanc, S. M. Clifford, K. Righter, and A. Hérique. Radar properties of comets: Parametric dielectric modeling of Comet. *Icarus*, 221:925–939, 2012.

E. Heggy, G. Scabbia, L. Bruzzone, and R. T. Pappalardo. Radar probing of Jovian icy moons: Understanding subsurface water and structure detectability in the JUICE and Europa missions. *Icarus*, 285:237–251, 2017. ISSN 10902643. doi: 10.1016/j.icarus.2016.11.039. URL `http://dx.doi.org/10.1016/j.icarus.2016.11.039`.

K. Kalousová, D. Schroeder, and K. Soderlund. Radar attenuation in Europa's ice shell: Obstacles and opportunities for constraining the shell thickness and its thermal structure. *J. Geophys. Res. Planets*, 122(3):524–545, 2017.

J. Kargel. Europa's crust and ocean: Origin, composition, and the prospects for life. *Icarus*, 148(1):226–265, 2000.

K. K. Kärkkäinen, A. H. Sihvola, and K. I. Nikoskinen. Effective Permittivity of Mixtures : Numerical Validation by the FDTD Method. *IEEE Transactions on Geoscience and Remote Sensing*, 38(3):1303–1308, 2000.

A. K. Kendrick, D. M. Schroeder, W. Chu, T. J. Young, P. Christoffersen, J. Todd, S. H. Doyle, J. E. Box, A. Hubbard, B. Hubbard, P. V. Brennan, K. W. Nicholls, and L. B. Lok. Surface Meltwater Impounded by Seasonal Englacial Storage in West Greenland. *Geophys. Res. Lett.*, 45(19):10,474–10,481, 2018. ISSN 19448007. doi: 10.1029/2018GL079787.

C. McCarthy, R. F. Cooper, S. H. Kirby, K. D. Rieck, and L. A. Stern. Solidification and microstructures of binary ice-I/hydrate eutectic aggregates. *Am. Mineral.*, 92(10):1550–1560, 2007. ISSN 0003004X. doi: 10.2138/am.2007.2435.

A. S. McEwen and E. B. Bierhaus. the Importance of Secondary Cratering To Age Constraints on Planetary Surfaces. *Annu. Rev. Earth Planet. Sci.*, 34(1):535–567, 2006. ISSN 0084-6597. doi: 10.1146/annurev.earth.34.031405.125018. URL `http://www.annualreviews.org/doi/10.1146/annurev.earth.34.031405.125018`.

B. McKinnon. Convective instability in Europa's floating ice shell. *Geophys. Res. Lett.*, 26 (7):951–954, 1999.

W. McKinnon. Radar sounding of convecting ice shells in the presence of convection: application to Europa, Ganymeded, and Callisto. *LPSC Abstr.*, 2005.

C. Michaut and M. Manga. Domes, pits, and small chaos on Europa produced by water sills. *J. Geophys. Res. E Planets*, 119(3):550–573, 2014. ISSN 21699100. doi: 10.1002/2013JE004558.

J. Moore. Models of Radar Absorption in Europan Ice. *Icarus*, 147(1): 292–300, 2000. ISSN 00191035. doi: 10.1006/icar.2000.6425. URL `http://linkinghub.elsevier.com/retrieve/pii/S001910350096425X`.

J. Mouginot, W. Kofman, A. Safaeinili, C. Grima, A. Herique, and J. J. Plaut. MARSIS surface reflectivity of the south residual cap of Mars. *Icarus*, 201

(2):454–459, 2009. ISSN 00191035. doi: 10.1016/j.icarus.2009.01.009. URL http://dx.doi.org/10.1016/j.icarus.2009.01.009.

C. S. Neal. The dynamics of the ross ice shelf revealed by radio echo-sounding. *J. Glaciol.*, 24:295–307, 1979.

R. T. Pappalardo and R. J. Sullivan. Evidence for separation across a gray band on Europa. *Icarus*, 123(2):557–567, 1996. ISSN 00191035. doi: 10.1006/icar.1996.0178.

J. G. Paren and G. Robin. Internal reflections in polar ice sheets. *J. Glaciol.*, 14(71):251–259, 1975.

M. Peters, D. Blankenship, and D. L. Morse. Analysis techniques for coherent airborne radar sounding: Application to West Antarctic ice streams. *J. Geophys. Res. Solid Earth*, 110 (6):1–17, 2005. ISSN 21699356. doi: 10.1029/2004JB003222.

E. Pettinelli, S. E. Lauro, B. Cosciotti, E. Mattei, F. Di Paolo, and G. Vannaroni. Dielectric characterization of ice/MgSO4.11H2O mixtures as Jovian icy moon crust analogues. *Earth Planet. Sci. Lett.*, 439:11–17, 2016. ISSN 0012821X. doi: 10.1016/j.epsl.2016.01.021. URL http://dx.doi.org/10.1016/j.epsl.2016.01.021.

C. B. Phillips and R. T. Pappalardo. Europa clipper mission concept: Exploring Jupiter's ocean moon. *Eos (Washington. DC).*, 95(20):165–167, 2014. ISSN 23249250. doi: 10.1002/2014EO200002.

O. Prieto-Ballesteros and J. Kargel. Thermal state and complex geology of a heterogeneous salty crust of Jupiter's satellite, Europa. *Icarus*, 173(1):212–221, 2005.

P. M. Saulnier, M. P. Zinkin, and G. H. Watson. Scatterer correlation effects on photon transport in dense random media. *Physical Review B*, 42(4):2621–2623, 1990.

B. E. Schmidt, D. D. Blankenship, G. W. Patterson, and P. M. Schenk. Active formation of 'chaos terrain' over shallow subsurface water on Europa. *Nature*, 479(7374):502–505, 2011. ISSN 00280836. doi: 10.1038/nature10608. URL `http://dx.doi.org/10.1038/nature10608`.

D. Schroeder, D. Blankenship, R. K. Raney, and C. Grima. Estimating subglacial water geometry using radar bed echo specularity: Application to Thwaites Glacier, West Antarctica. *IEEE Geosci. Remote Sens. Lett.*, 2015. ISSN 1545598X. doi: 10.1109/LGRS.2014.2337878.

D. M. Schroeder, A. Romero-Wolf, L. Carrer, C. Grima, B. A. Campbell, W. Kofman, L. Bruzzone, and D. Blankenship. Assessing the potential for passive radio sounding of Europa and Ganymede with RIME and REASON. *Planet. Space Sci.*, 134(October):52–60, 2016. ISSN 00320633. doi: 10.1016/j.pss.2016.10.007. URL `http://dx.doi.org/10.1016/j.pss.2016.10.007`.

R. A. Simpson. Electromagnetic reflection and transmission at interfaces involving graded dielectrics with applications to planetary radar astronomy. *IEEE Trans. Anten. Propag*, AP-24:17–24, 1976.

K. N. Singer, W. B. MicKinnon, and P. Schenk. Pits, spots, uplifts, and small chaos regions on Europa: Evidence for diapiric upwelling from morphology and morpometry. *LPSC Abstr.*, 2010.

I. B. Smith, N. E. Putzig, J. W. Holt, and R. J. Phillips. An ice age recorded in the polar deposits of Mars. *Science*, 352:1075–1078, 2016. ISSN 0036-8075. doi: 10.1126/science.aad6968.

N. A. Spaun and J. W. Head. A model of Europa's crustal structure' Recent Galileo results and implications for an ocean. *J. Geophys. Res.*, 106:7567–7576, 2001.

R. Thomson and J. R. Delaney. Evidence for a weakly stratified Europan ocean sustained by seafloor heat flux. *J. Geophys. Res.*, 106(2000):12355, 2001. ISSN 0148-0227. doi: 10.1029/2000JE001332.

L. Tsang and J. Kong. *Scattering of Electromagnetic Waves: Advanced Topics*. Wiley Series in Remote Sensing and Image Processing. Wiley, 2004. ISBN 9780471463795. URL https://books.google.com/books?id=asPo5MMgzyUC.

L. Tsang, J. Kong, and R. Shin. *Theory of Microwave Remote Sensing*. Wiley Series in Remote Sensing and Image Processing. Wiley, 1985. ISBN 9780471888604. URL https://books.google.com/books?id=B88PAQAAIAAJ.

F. T. Ulaby and G. Long. *Microwave Radar and Radiometric Remote Sensing*, volume 4. University of Michigan Press Ann Arbor, 2014.

F. Wilhelms. Explaining the dielectric properties of firn as a density-and- conductivity mixed permittivity (DECOMP). *Geophysical Research Letters*, 32:4–7, 2005. doi: 10.1029/2005GL022808.